

Asociación Argentina
de Mecánica Computacional



Mecánica Computacional Vol XXXV, págs. 329-347 (artículo completo)
Martín I. Idiart, Ana E. Scarabino y Mario A. Storti (Eds.)
La Plata, 7-10 Noviembre 2017

PARAMETERIZED CELLULAR MATERIAL FOR THE ELASTIC MIMETIZATION OF CANCELLOUS BONE

Lucas Colabella^a, Adrián P. Cisilino^{a*}, Guillaume Häiat^b and Piotr Kowalczyk^c

^a *División Mecánica de Materiales, INTEMA, Facultad de Ingeniería, Universidad Nacional de Mar del Plata, Av. Juan B. Justo 4302, 7600 Mar del Plata, Argentina, cisilino@fi.mdp.edu.ar.*

^b *Laboratoire Modélisation et Simulation Multiéchelle, CNRS 8208, CNRS, 61 Avenue du General de Gaulle, 94010 Creteil, France.*

^c *Institute of Fundamental Technological Research, Polish Academy of Sciences, Pawinskiego 5B, 02-106 Warsaw, Poland*

Keywords: Biomimetism, Parameterized microstructures, Symmetry classes.

Abstract. Bone tissue mechanical properties and trabecular microarchitecture are the main factors that determine the biomechanical properties of cancellous bone. Artificial cancellous microstructures, typically described by a reduced number of geometrical parameters, can be designed to obtain a mechanical behavior mimicking that of natural bone. In this work, we assess the ability of the parameterized microstructure introduced by Kowalczyk (P. Kowalczyk, *Comput Meth Biomech Biomed Eng*, 9:135–147, 2006) to mimic the elastic response of cancellous bone. An optimization approach is devised to find the geometrical parameters of the artificial microstructure that better mimics the elastic response of target natural bone specimen. This is done via a Pattern Search algorithm that minimizes the difference between the symmetry class decompositions of the elastic tensors. The performance of the method is demonstrated via analyses for 146 bone samples.

1 INTRODUCTION

Bones are hierarchical bio-composite materials with a complex multiscale structural geometry (Carretta et al. 2013). Bone tissue is arranged either in a compact pattern (cortical bone) or a spongy pattern (cancellous bone). Cancellous bone can be found in vertebral bodies and at the epiphyses of long bones. In the vertebral body, it is the main load bearing structure, whereas in the appendicular skeleton, it transfers mechanical loads from the articular surface to cortical bone. Cancellous bone can be assimilated to a nanocomposite material with hierarchical structure. In a bottom-up description, the structure starts in the nanoscale (mineralized collagen fibril) and moves up to the sub-microscale (single lamella), the microscale (single trabecula), and mesoscale (trabecular bone) levels. Trabeculae are organized into a three-dimensional lattice oriented mainly along the lines of stress, which forms a stiff and ductile structure that provides the framework for the soft bone marrow filling the intertrabecular spaces.

Different experiments have shown that linear elasticity can predict the behavior of cancellous bone (Keaveny et al. 1994). The trabecular architecture determines the elastic anisotropy of cancellous bone, which can be described by a fourth rank elastic tensor, which linearly relates stress and strains. The elastic tensor is determined in its most general form by 81 components. Cancellous bone is generally assumed to behave as an orthotropic structure in the mesoscale, with three planes of symmetry, what requires of only nine independent components to fully describe the elastic behavior of the structure (Yang et al., 1998).

Large-scale finite-element (FE) homogenization analyses of microstructural models built from micro-computed tomographic scans of real bone specimens allow for the computation of the cancellous-bone effective elastic properties. Finite element analyses solve some of the drawbacks of the experimental techniques, since FE models can be subjected without restrictions to the load conditions needed to evaluate the anisotropic behavior of the microstructure. FEA has been applied to large sets of data to find the orthotropic components of cancellous bone (Kabel et al. 1999a, 1999b), which show that there are strong correlations between the bone volume fraction and elastic and shear moduli, whereas this correlation is weak for the Poisson's ratio.

Another approach is to use parametric models of trabecular bone, which consist in artificial microstructures formed by plates and rods. Artificial microstructures may be criticized for being somewhat unrealistic, however, their main advantage is that the mesoscopic properties characterizing such microstructures can be expressed as explicit continuous functions of some well-defined geometrical parameters. Moreover, it has been found that models based on local morphometry, composed of individual rods and plates, help improving the understanding of local structural changes in the determination of bone stiffness (Stauber and Müller, 2006a, 2006b). Explicit relations between geometrical parameters and mesoscopic properties are crucial for modeling the microstructure evolution at the large scale; they allow to formulate the problem as merely the evolution of a set of scalar variables, which is much more efficient in terms of computational cost than the analysis of the geometric evolution of certain components of micro-CT-based actual bone microstructures. An example in this sense is the artificial trabeculae developed by Kowalczyk (2006), which have been successfully employed in the modeling of long-term changes in morphological and mechanical properties of trabecular bone in the proximal femur (Kowalczyk, 2010).

In this work the parameterized cancellous microstructure introduced by Kowalczyk (2006) is analyzed in terms of its ability to mimic the elastic response of natural cancellous bone. Artificial microstructures are compared with actual bone samples in terms of their symmetry classes and their elasticity matrices represented in terms of the geometrical parameters. An optimization scheme is proposed to determine the values of the parameters that result in the

microarchitecture that best mimics the elastic response of a target natural bone specimen. The optimization scheme uses a Pattern Search algorithm to minimize the difference between the elastic symmetry classes of artificial and natural microstructures.

2 ELASTIC PROPERTIES OF CANCELLOUS BONE

2.1 Experimental data

The database by [Kabel et al. \(1999a, 1999b\)](#) provides the entire set of anisotropic elastic constants of 141 human cancellous-bone specimens of vertebral body, calcaneus, proximal tibia and distal femur. Specimen bone volume-to-total volume ratios cover the range $5\% \leq BV/TV \leq 35\%$. The elastic constants are the results of finite element (FE) homogenization analyses performed on computer reconstructions of the specimen microarchitectures. Linear elastic and isotropic material properties were specified for the bone tissue, with a Young's modulus of $E = 1$ GPa and Poisson's ratio $\nu = 0.3$, so the homogenized results can be scaled for any value of the tissue modulus. The specimen imaging and homogenization procedures are fully described in [Kabel et al. \(1999b\)](#).

2.2 Elastic symmetry analyses

Elasticity tensors can be decomposed into sums of orthogonal tensors belonging to the different symmetry classes. We use for this purpose the method by [Browaeys and Chevrot \(2004\)](#). This method relies on the following vectorial description of the elasticity tensor,

$$\mathbf{X} = (C_{11}, C_{22}, C_{33}, \sqrt{2}C_{23}, \sqrt{2}C_{13}, \sqrt{2}C_{12}, 2C_{44}, 2C_{55}, 2C_{66}, 2C_{14}, 2C_{25}, 2C_{36}, 2C_{34}, 2C_{15}, 2C_{26}, 2C_{24}, 2C_{35}, 2C_{16}, 2\sqrt{2}C_{56}, 2\sqrt{2}C_{46}, 2\sqrt{2}C_{45}), \quad (1)$$

where C_{ij} are the components of the elastic tensor \mathbb{C} in the Voigt notation. The normalization factors in the above expression are included so that the Euclidean norm of an arbitrary elastic tensor \mathbb{C} and its associated elastic vector \mathbf{X} are identical.

The vector description of the elastic tensor possesses the property that any symmetry class constitutes a subspace of a class of lower symmetry and an orthogonal projection on this subspace removes the lower symmetry part. Thus, when expressed in the so-called symmetry Cartesian coordinate system (see [Cowin and Mehrabadi, 1987](#)), \mathbf{X} can be decomposed by a cascade of projections into a sum of vectors belonging to the symmetry classes triclinic, monoclinic, orthorhombic, tetragonal, hexagonal and isotropic:

$$\mathbf{X} = \mathbf{X}_{tri} + \mathbf{X}_{mon} + \mathbf{X}_{ort} + \mathbf{X}_{tet} + \mathbf{X}_{hex} + \mathbf{X}_{iso}. \quad (2)$$

The different elastic symmetry parts can be presented as fractions of the Euclidian norm of the elasticity vector such that

$$c_{iso} + c_{hex} + c_{tet} + c_{ort} + c_{mon} + c_{tri} = 1. \quad (3)$$

Computations for the determination of the symmetry Cartesian coordinate system, the transformations into vector forms, the symmetry decompositions and the normalizations were performed using the Matlab Seismic Anisotropy Toolkit (MSAT) by [Walker and Wookey \(2012\)](#).

Figure 1 presents the results for the symmetry class decompositions of the 141 human bone

samples in Kabel et al. (1999a, 1999b). The cumulative decompositions in (3) are presented as functions of the sample BV/TV . Table 3 summarizes the extreme values for the symmetry classes. It is observed from Figure 1 that the isotropic class accounts for the most significant fraction of the elasticity matrices over the complete BV/TV range. Although its wide dispersion, the mean value of the isotropic fraction increases linearly with BV/TV , from $\overline{c_{iso}} = 0.49$ for $BV/TV = 5\%$ to $\overline{c_{iso}} = 0.69$ for $BV/TV = 35\%$. Its standard deviation is $SD_{iso} = 0.12$. The second relevant fraction is for the hexagonal class. Conversely to the isotropic class, the mean value of the hexagonal class decreases linearly with BV/TV . The isotropic and hexagonal classes behave such that they add a constant, $\overline{c_{iso}} + \overline{c_{hex}} \cong 0.83$, with a standard deviation $SD_{iso+hex} = 0.07$. The tetragonal class fraction is marginal; around 1% for nearly 98% of the samples. The orthorhombic class presents a wide dispersion, but its mean value is nearly constant $\overline{c_{ort}} \cong 0.10$. The orthotropic symmetry,

$$c_{ortho} = c_{ort} + c_{tet} + c_{hex} + c_{iso}, \quad (4)$$

presents a constant average value $\overline{c_{ortho}} = 0.93$ with $SD_{ortho} = 0.04$. This last result is consistent with the observation by Yang et al. (1998), who found that \mathbb{C} matrices present orthotropic symmetry with a 95% confidence level.

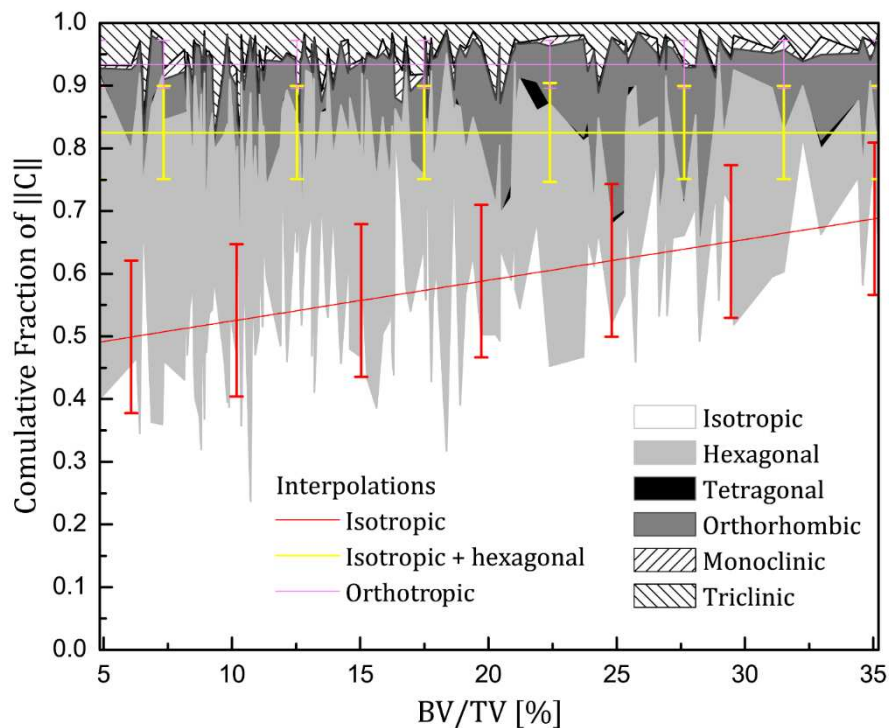


Figure 1: Symmetry class decomposition of the elasticity matrices of the 141 human-bone specimens reported by Kabel et al. (1999a, 1999b). Error bars indicate the standard deviations from the interpolated mean values.

Symmetry class	Human Samples Kabel et al. (1999a, 1999b)		Parameterized Kowalczyk (2006)	
	Min	Max	Min	Max
c_{iso}	0.24	0.84	0.36	1.00
c_{hex}	0.02	0.65	0.00	0.49
$c_{iso} + c_{hex}$	0.56	0.95	0.46	1.00
c_{tet}	0.00	0.05	0.00	0.15
c_{ort}	0.00	0.33	0.00	0.50
c_{ortho}	0.81	0.99	1.00	1.00
c_{mon}	0.00	0.08	-	-
c_{tri}	0.01	0.19	-	-

Table 1: Extreme values of the symmetry classes of the natural and parameterized trabecular microstructures.

3 A MIMETIC CANCELLOUS BONE MICROSTRUCTURE

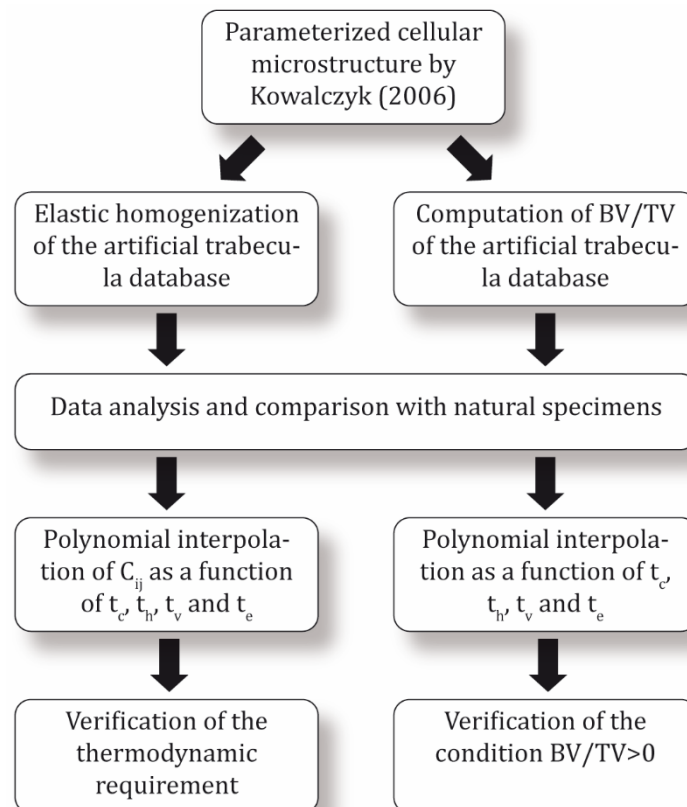


Figure 2: Workflow of the development of a mimetic cancellous bone microstructure.

The workflow in Figure 2 depicts the procedure for the development of the mimetic cancellous bone microstructure. The first step is the computation of the elasticity and BV/TV data of the parameterized cellular microarchitecture introduced by Kowalczyk (2006), on which the development is based. The capabilities of the parameterized microstructure to mimic natural bone is assessed through the comparison and correlation of the elastic and BV/TV data with that of the natural specimens. Next, the elastic and BV/TV data are interpolated as functions of the geometrical parameters. These interpolations will play a key role in the implementation of

the optimization algorithm. Finally, the polynomial interpolations are checked for consistency. The details of this procedure are given next.

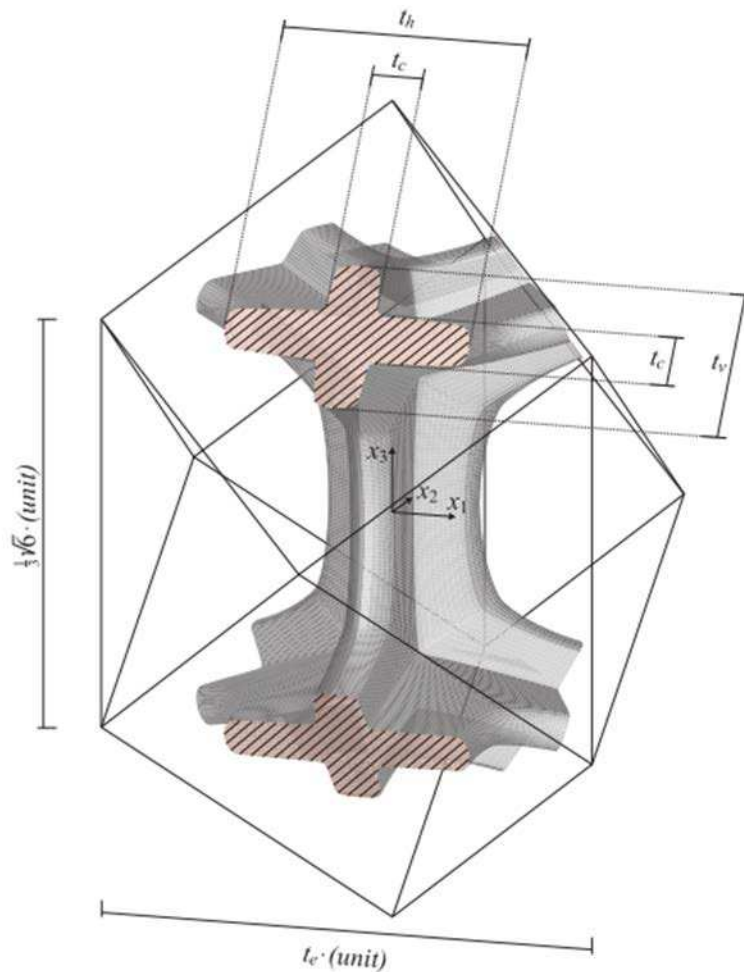


Figure 3: Geometry of a repeatable cell.

3.1 The parameterized cellular microstructure

The parameterized cellular microarchitecture introduced by Kowalczyk (2006) is shown in Figure 3. It consists in a repeatable cell that is inscribed into a space-filling dodecahedron, so it can be arranged in rows and layers to completely fill the 3-D space. The geometry of the cell is described by Bezier curves and corresponding surface patches. Surface transitions between neighboring cells are smooth. Shaded areas denote trabecular surface while the hatched areas are the cross-sections at which the cell is “stuck” to identical neighboring cells.

The repeatable geometry is described in terms of four geometrical parameters: t_c , t_h and t_v , which define proportions between trabecular plate widths and thicknesses to produce transversely isotropic microstructures in the $x_1 - x_2$ plane; and t_e , which scales it in the x_1 direction to produce fully orthotropic microstructures. Parameters t_c , t_h and t_v are non-dimensional as they are understood as fractions of the corresponding cell dimensions and may take values between 0 and 1. To produce feasible geometries, they must comply with the restrictions

$$t_h \geq t_c, \quad t_v \geq t_c. \quad (5)$$

Parameter values can be set to produce microstructures with solid volume fractions in the range $0 < BV/TV < 100\%$.

3.2 Homogenization analysis and comparison with natural specimens

Kowalczyk (2006) used FE homogenization to compute the elasticity matrices for a broad set of microstructures given by (t_c, t_h, t_v, t_e) quadruplets on the domains $t_c \in (0,1)$, $t_h \in [t_c, 1)$ and $t_v \in [t_c, 1)$ in increments of 0.05, $t_e \in [0.6,1.4]$ in increments of 0.2, and elastic properties $E = 1$ GPa and $\nu = 0.3$. From the comparison of the obtained effective elastic constants to those of the natural samples by Kabel et al. (1999a, 1999b), he showed that individual ranges of E_{ij} , G_{ij} and ν_{ij} of the parameterized microstructures are always wider than those of the natural specimens for every BV/TV value. This is justified since some combinations of parameters (t_c, t_h, t_v, t_e) may occur seldom in reality or be unrealistic at all.

In what follows, the above analysis is extended to assess the capability of the parameterized microstructure to mimic the natural elastic symmetries. To this end, the database of elastic constants for the parameterized microstructure was refined, such that the four geometric parameters were varied in increments of 0.05. The FE homogenization procedure of Kowalczyk (2006) was used for the computation of the effective elastic constants. The repeatable cells that results for each combination of the geometric parameters were discretized with 8-node linear brick elements and appropriate boundary conditions that ensure fitting of all deformed neighboring cells to each other were specified. Six load cases were considered for each cell: pure stretching in three orthogonal directions x_1, x_2, x_3 (see Figure 3) and pure shear in three orthogonal planes (normal to the three directions), which were specified in terms of the displacement fields. Reaction forces were measured for each case and used to compute the elements of the elasticity matrix. Thus, the construction of the database consisted of 41,990 homogenization analysis that involved the solution of approximately 250,000 finite-element models altogether.

Stiffness matrices of the parameterized microstructures are decomposed into their symmetry classes using the same procedure introduced earlier for the natural specimens. The extreme values attained by the symmetry classes are reported in Table 1. It is found that the parameterized microstructure covers the complete extents of the tetrahedral and orthorhombic classes of the natural specimens. On the other hand, it fails to cover the lowermost values of the isotropic class, $0.24 \leq c_{iso} < 0.36$, and the uppermost values of the hexagonal class, $0.49 > c_{hex} \geq 0.65$ for the human specimens. However, it is worth noting that only a few samples lie within the excluded ranges: 5 samples have $c_{iso} < 0.36$ and 2 samples have $c_{hex} > 0.49$, i.e., less than 5% of the 141 samples in the database. Symmetry classes of the bovine samples lie always within the extents of the parameterized microstructure.

The capability of the parameterized microstructure to mimic the elastic behavior is further assessed in terms of BV/TV . Figure 4 shows the symmetry classes of the parameterized microstructures for the range of BV/TV of the natural samples; these are 17,522 data points (to keep the figure clear not all data points were plot). Results are presented for c_{iso} , $c_{iso} + c_{hex}$ and c_{ortho} in subfigures (a), (b) and (c), respectively. The corresponding data for the natural samples are also shown in the figures: gray areas indicate the standard deviation of the human samples (see Figure 1) while the square marks are the values of the bovine samples (see Figure 1). Figure 4(a) shows that with the only exception of the lowermost values, i.e., for $5\% \lesssim BV/TV \lesssim 7\%$, the parameterized microstructure can mimic the isotropic class of the natural trabeculae. Regarding $c_{iso} + c_{hex}$, Figure 4(b) shows that the parameterized microstructure completely encompasses the data of the natural samples (the gray area is hardly visible behind the symbols). Finally, the results for the orthotropic symmetry in Figure 4(c)

show that, consistently with its geometric definition, the parameterized microstructure shows $c_{\text{ortho}} = 1$ over the complete BV/TV range, which results in a consistent overestimation of the orthotropic symmetry by the parameterized microstructure, the mean value and standard deviation of which is $6.6 \pm 3.8\%$ with respect to the human samples. Regarding the bovine samples, the overestimation ranges from 9% to 19%.

3.3 Polynomial interpolation

The discrete elastic-constant and symmetry-class data of the parameterized microstructures were examined to investigate their functionalities with the geometric parameters.

It was observed that coefficients of the stiffness tensor \mathbb{C} behave as continuous and smooth functions of t_c , t_h , t_v and t_e over the complete range, and that in general, the C_{ij} rise with the increment of the geometrical parameters. As examples, Figure 5 illustrates the behaviors of C_{11} and C_{12} as functions of t_v and t_c for $t_h = 0.6$ and $t_e = 1.2$.

On the other hand, symmetry classes showed to be, in some cases, discontinuous functions of the geometric parameters. Figure 6 depicts the changes of the symmetry classes associated to the variation of the elasticity coefficients given in Figure 5. It can be observed that, although \mathbb{C} coefficients have a continuous variation, the hexagonal, tetragonal and orthorhombic symmetries present discontinuities.

Based on the above observations, the discrete elastic-constant data was used to interpolate an analytical expression for $\mathbb{C}(t_c, t_h, t_v, t_e)$. The nine non-zero coefficients, C_{11} , C_{22} , C_{33} , C_{12} , C_{13} , C_{23} , C_{44} , C_{55} and C_{66} , were interpolated polynomially by means of least-square fitting. Polynomials of order 5 to 12 were used; the quality of the interpolations was assessed in terms of the coefficient of determination (R2), the root-mean-square error (RMSE) and the residual sum of squares (SSres).

Since the C_{ij} were interpolated separately, the thermodynamic requirement for $\mathbb{C}(t_c, t_h, t_v, t_e)$ was checked. The thermodynamic requirement (positive definiteness of strain energy) enforces the condition that the invariants of the elasticity matrix should be positive, or in other words, that both, $\mathbb{C}(t_c, t_h, t_v, t_e)$ and its inverse must be positive definite. These conditions were verified for the interpolated $\mathbb{C}(t_c, t_h, t_v, t_e)$ for quadruplets in the intervals $t_c \in [0.05, 0.95]$, $t_h \in [t_c, 0.95]$, $t_v \in [t_c, 0.95]$ and $t_e \in [0.6, 1.4]$ in increments of 0.01. The thermodynamic requirement was found valid on most of the interpolation range. Polynomial fittings of order 10 are selected, since they produce accurate and valid interpolations over a wide range of the parameter values that allows for solid volume fractions $1\% \leq BV/TV \leq 99\%$.

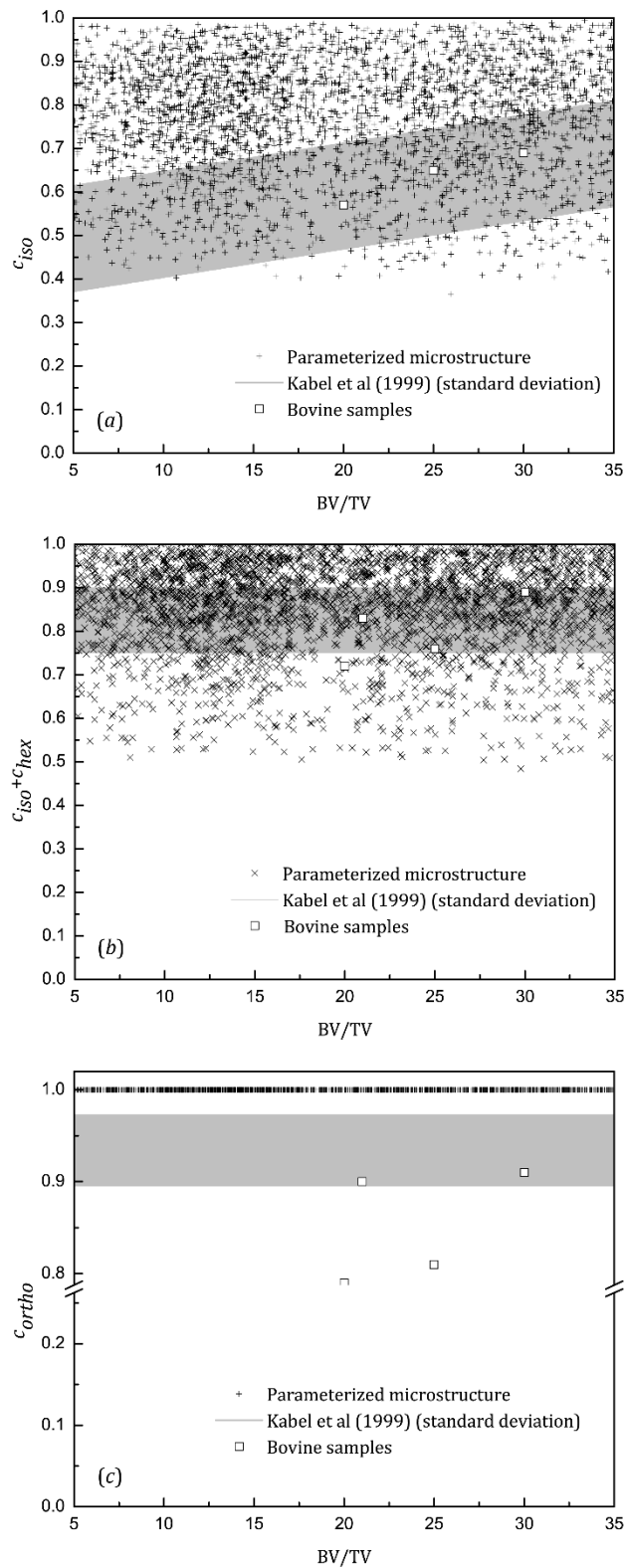


Figure 4: Comparison of elastic symmetry classes of the natural and the parameterized trabecular microstructures: (a) isotropic class, (b) isotropic + hexagonal classes, (c) orthotropy.

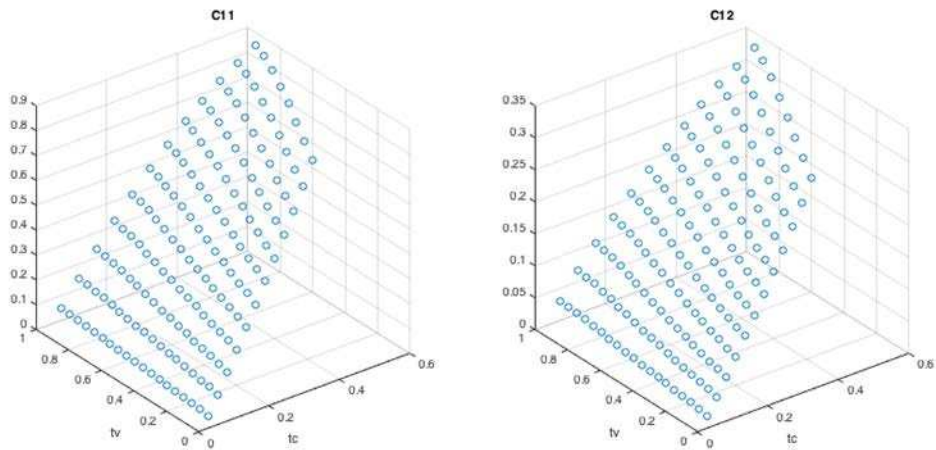


Figure 5: Parameterized-microstructure elasticity coefficients C_{11} and C_{12} as functions of t_c and t_v for $t_h = 0.6$ and $t_e = 1.2$.

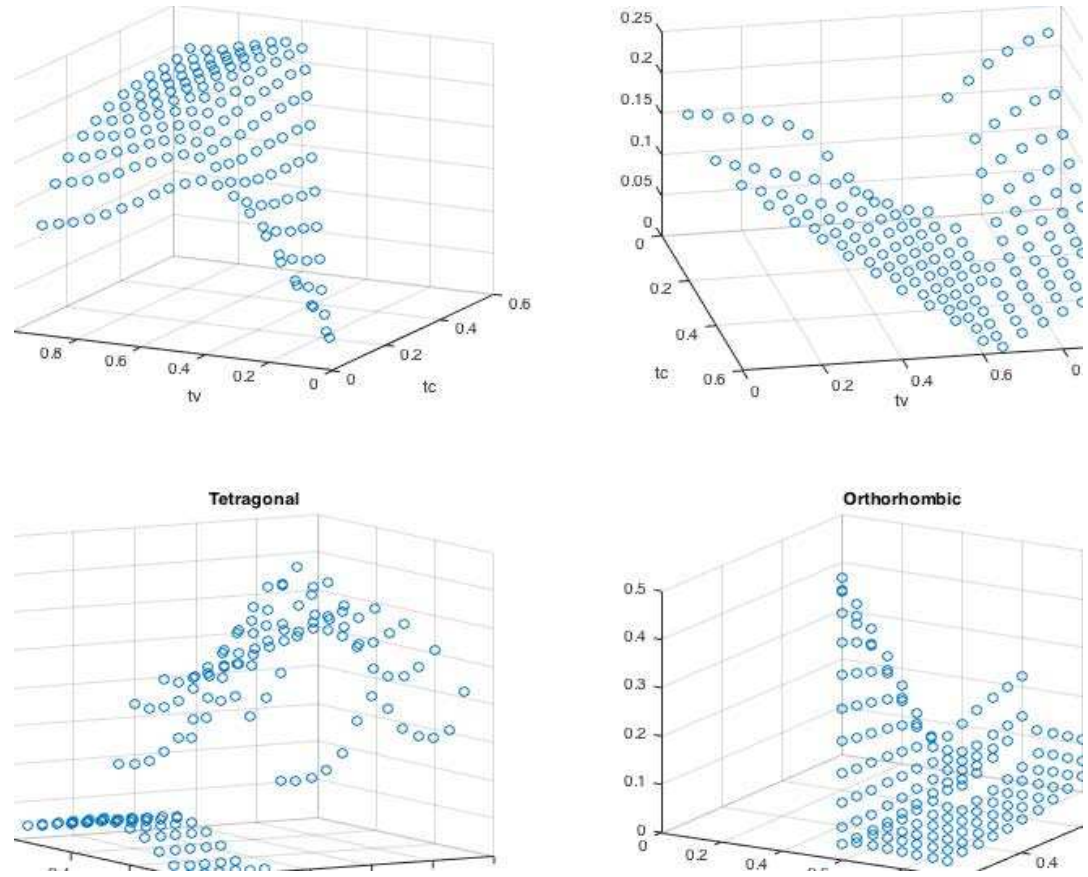


Figure 6: Parameterized-microstructure symmetry classes as functions of t_v and t_c for $t_h = 0.6$ and $t_e = 1.2$.

4 OPTIMIZATION

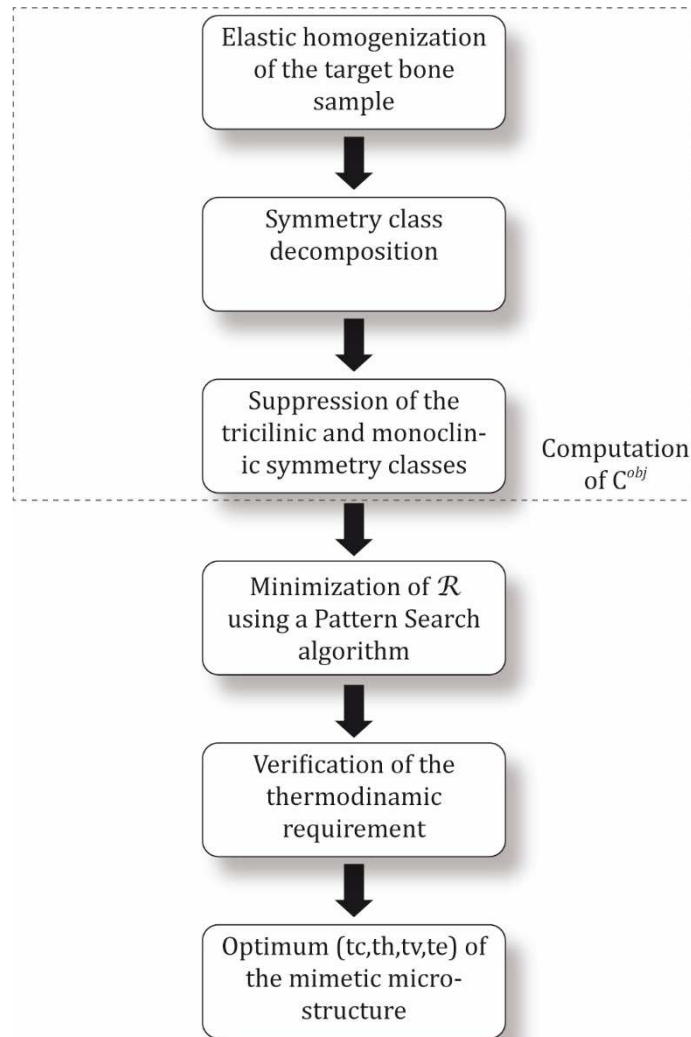


Figure 7: Workflow of the optimization analysis.

4.1 Problem statement

The optimization problem is to find the parameterized microstructure that better mimics the elastic response of a target natural bone specimen. The elastic equivalence among the microstructures is posed in terms of the symmetry classes.

The workflow is illustrated in Figure 7. The analysis starts with the elastic homogenization of the target bone sample; the resultant elasticity matrix is decomposed into symmetry classes. The triclinic and monoclinic classes are suppressed to obtain the target elasticity matrix. Thus, the resultant $\mathbb{C}^{\text{target}}$ has orthotropic symmetry, and it is compatible with the artificial microstructure.

The problem consists in finding the quadruplet t_c , t_h , t_v and t_e that minimizes the overall difference between the symmetry class decompositions:

$$\mathcal{R} = \min \sqrt{\begin{matrix} (c_{iso}^{target} - c_{iso})^2 + (c_{hex}^{target} - c_{hex})^2 \\ + (c_{tet}^{target} - c_{tet})^2 + (c_{ort}^{target} - c_{ort})^2 \end{matrix}}, \quad (6)$$

where c_{iso}^{target} , c_{hex}^{target} , c_{tet}^{target} , c_{ort}^{target} and c_{iso} , c_{hex} , c_{tet} , c_{ort} are the normalized symmetry classes of the target and the parameterized microstructures, respectively; c_{iso} , c_{hex} , c_{tet} and c_{ort} are functions of t_c , t_h , t_v and t_e .

Geometric parameters are subjected to the inequality restrictions in equation (5) and at the same time, they must comply with the restriction imposed by the bone volume-to-total volume ratio of the target microstructure,

$$BV/TV(t_c, t_h, t_v, t_e) = BV/TV^{target}, \quad (7)$$

Alternatively, the restriction of the bone volume-to-total volume ratio might be relaxed, such as

$$\begin{aligned} BV/TV^{target} (1 - BV/TV_{tol}) &\leq BV/TV(t_c, t_h, t_v, t_e) \\ &\leq BV/TV^{target} (1 + BV/TV_{tol}), \end{aligned} \quad (8)$$

where BV/TV_{tol} is a prescribed tolerance that could take any value in the interval $[0,1]$.

4.2 Algorithm

The optimization problem is solved using the derivative-free constrained direct search solver pattern search (PS) of the Matlab Global Optimization Toolbox. The PS is selected because being derivative-free, it can deal with the discontinuous functionalities between the symmetry classes and the geometrical parameters, see Section 3.3. `patternsearch` computes a sequence of points that approach an optimal of

$$\min_x f(x) \text{ such that } \begin{cases} c_{eq}(x) = 0 \\ c_{ineq}(x) \leq 0 \\ A_{ineq}(x) \cdot x \leq b_{ineq} \\ b_{low} \leq x \leq b_{up} \end{cases} \quad (9)$$

where $x = [t_c, t_h, t_v, t_e]^T$ and the objective function is $f(x) = \mathcal{R}(t_c, t_h, t_v, t_e)$. At each step, the algorithm searches a set of points, called a mesh, around the current point. The mesh is formed by adding the current point to a scalar multiple of a set of vectors called a pattern. If the pattern search algorithm finds a point in the mesh that improves the objective function at the current point, the new point becomes the current point at the next step of the algorithm.

The constrain functions are used for the restriction on BV/TV . In the case of a prescribed target BV/TV , the equality function constrain, $c_{eq}(x) = 0$, is

$$BV/TV(t_c, t_h, t_v, t_e) - BV/TV^{target} = 0, \quad (10)$$

while if BV/TV is defined as in equation (8), two $c_{ineq}(x) \leq 0$ are specified:

$$BV/TV(t_c, t_h, t_v, t_e) - BV/TV^{target} (1 + BV/TV_{tol}) \leq 0 \quad (11)$$

and

$$BV/TV^{target} (1 - BV/TV_{tol}) - BV/TV(t_c, t_h, t_v, t_e) \leq 0. \quad (12)$$

Inequality constrains are the restrictions on the geometric parameters in equation (5). Thus, $A_{ineq}(x) \cdot x \leq b_{ineq}$ is

$$\begin{bmatrix} 1 & -1 & 0 & 0 \\ 1 & 0 & -1 & 0 \end{bmatrix} \begin{bmatrix} t_c \\ t_h \\ t_v \\ t_e \end{bmatrix} \leq \begin{bmatrix} 0 \\ 0 \end{bmatrix}. \quad (13)$$

Finally, inequality constrains $b_{low} \leq x \leq b_{up}$ are used to set the validity intervals for the polynomial interpolations in Section 3.2. These are

$$b_{low} = \begin{bmatrix} 0.06 \\ 0.06 \\ 0.06 \\ 0.6 \end{bmatrix} \text{ and } b_{up} = \begin{bmatrix} 0.95 \\ 0.95 \\ 0.95 \\ 1.4 \end{bmatrix}. \quad (14)$$

Stopping criteria involves tolerances for `FunctionTolerance`, the difference between the function value at the previous best point and function value at the current best point; `MeshTolerance`, the minimum size for the search mesh; and `StepTolerance`, the minimum distance from the previous best point to the current best point. The three tolerances were set with the default values of 10^{-6} .

4.3 Verification and tuning

The optimization procedure was verified, tested and tuned by assessing its effectiveness to identify microstructures among those of the database used for the elasticity-matrix polynomial fitting (see Section 3.3). To this end, 100 parameterized microstructures were randomly selected from the database to serve as target microstructures. Problems were solved for $BV/TV_{tol} = 1\%$ and 5% . Since the thermodynamic requirement was checked only for discrete combinations (t_c, t_h, t_v, t_e) in Section 3.3, there is no guarantee that all possible combinations will satisfy it. Therefore, the thermodynamic requirement for $\mathbb{C}(t_c, t_h, t_v, t_e)$ was checked at the end of each optimization procedure.

Preliminary tests had shown that the performance of the algorithm was sensitive to the initial values (seeds) of the geometric parameters. Thus, each problem was run four times for different sets of random seeds and the best result reported.

Table 2 reports the mean values of the residuals and the mean values and standard deviations of the relative errors of the geometric parameters and the symmetry classes. Errors for the geometric parameters are

$$e_{t_c} = \frac{t_c - t_c^{target}}{t_c^{target}}, \quad e_{t_h} = \frac{t_h - t_h^{target}}{t_h^{target}}, \quad (15)$$

$$e_{t_v} = \frac{t_v - t_v^{otarget}}{t_v^{target}} \quad \text{and} \quad e_{t_e} = \frac{t_e - t_e^{target}}{t_e^{target}}.$$

Besides, errors for the symmetry classes are relative to the corresponding average value of the 100 target microstructures. This approach avoids the occurrence of boundless and misleading large errors for the target microstructures with zero or nearly zero symmetry classes. Thus, the errors for the symmetry classes are defined as follows

$$\begin{aligned} e_{c_{iso}} &= \frac{c_{iso} - c_{iso}^{target}}{c_{iso}^{target}}, & e_{c_{hex}} &= \frac{c_{hex} - c_{hex}^{target}}{c_{hex}^{target}}, \\ e_{c_{tet}} &= \frac{c_{tet} - c_{tet}^{target}}{c_{tet}^{target}} \quad \text{and} \quad e_{c_{ort}} &= \frac{c_{ort} - c_{ort}^{target}}{c_{ort}^{target}}, \end{aligned} \quad (16)$$

where $\overline{c_{iso}^{target}}$, $\overline{c_{hex}^{target}}$, $\overline{c_{tet}^{target}}$ and $\overline{c_{ort}^{target}}$ are the mean values of the symmetry class fractions for the target microstructures.

BV/TV_{tol} [%]	Residual	Error geom. parameters [%]				Symmetry-class errors x 10 ⁻³			
		t_c	t_h	t_v	t_e	c_{iso}	c_{hex}	c_{tet}	c_{ort}
0	1.4×10^{-2}	$17 \pm$	$-0 \pm$	$0 \pm$	$2 \pm$	$-4.8 \pm$	7 ± 237	$80 \pm$	$14 \pm$
		41	38	33	31	18.3		502	137
1	5.6×10^{-3}	$12 \pm$	$1 \pm$	$-5 \pm$	$4 \pm$	$0.7 \pm$	$18 \pm$	$-33 \pm$	$-0.4 \pm$
		33	34	18	25	11.7	168	262	47.9
5	3.1×10^{-3}	$5 \pm$	$4 \pm$	$6 \pm$	$5 \pm$	$-0.8 \pm$	$-1.4 \pm$	$27 \pm$	10 ± 66
		37	36	36	26	4.2	88.9	175	

Table 2: Mean values of the residuals and errors for the geometric parameters and the symmetry classes.

Table 2 shows that results are accurate for the symmetry classes, with maximum errors of a few percent for e_{tet} . Error e_{tet} diminishes from 8% to 3% with the increment of BV/TV_{tol} . However, this is not the case for all the symmetry classes; note that e_{hex} and e_{ort} present their minima for $BV/TV_{tol} = 1\%$. Maximum standard deviations are also for e_{tet} , and they reduce from 50% to 17% with the increment of BV/TV_{tol} . The largest error in the geometric parameters is for t_c , which diminishes from 17% to 5% as the tolerance for the bone volume fraction is relaxed from $BV/TV_{tol} = 0$ to $BV/TV_{tol} = 5\%$. In contrast, minimum errors for t_h , t_v and t_e are for $BV/TV_{tol} = 0$, and they deteriorate with BV/TV_{tol} ; in any case, maximum errors are of a few percent. The standard deviations for the geometric parameters are not sensitive to BV/TV_{tol} and they are from 25% to 40%.

The mean BV/TV of the optimal microstructures are very close the target values; mean values for the relative error

$$e_{BV/TV} = \frac{BV/TV - BV/TV^{target}}{BV/TV^{target}} \quad (17)$$

are $\overline{e_{BV/TV}} = 7 \cdot 10^{-4}$ and $-5 \cdot 10^{-3}$ for $BV/TV_{tol} = 1\%$ and 5% , respectively.

5 APPLICATION TO NATURAL TRABECULAR SAMPLES

5.1 Human specimens

Elasticity matrices of the 141 human bone samples were filtered to retrieve their orthotropic parts. To do so, components $C_{14}, C_{15}, C_{16}, C_{24}, C_{25}, C_{26}, C_{34}, C_{35}, C_{36}, C_{45}, C_{46}$ and C_{56} were set equal to zero for the elastic tensors oriented in the symmetry Cartesian coordinate system and their symmetry class decompositions computed such that $c_{ort}^{obj} + c_{tet}^{obj} + c_{hex}^{obj} + c_{iso}^{obj} = 1$. The resultant data was used as target values for the optimization procedure. Optimizations were performed for $BV/TV_{tol} = 0\%, 1\%, 5\%$ and 10% .

Symmetry classes for the obtained effective elastic properties are assessed in relation to the mean values of their extreme fractions for the human microstructures in Table 1, this is:

$$e'_{c_{iso}} = \frac{c_{iso} - c_{iso}^{target}}{\frac{1}{2}(c_{iso}^{max} + c_{iso}^{min})}, \quad e'_{c_{hex}} = \frac{c_{hex} - c_{hex}^{target}}{\frac{1}{2}(c_{hex}^{max} + c_{hex}^{min})},$$

$$e'_{c_{tet}} = \frac{c_{tet} - c_{tet}^{target}}{\frac{1}{2}(c_{tet}^{max} + c_{tet}^{min})} \text{ and } e'_{c_{ort}} = \frac{c_{ort} - c_{ort}^{target}}{\frac{1}{2}(c_{ort}^{max} + c_{ort}^{min})}. \quad (18)$$

Results showed no significant improvements with the relaxation of the BV/TV_{tol} constrain, so only the results for $BV/TV_{tol} = 1\%$ are presented next. Mean errors for 141 samples are $\overline{e'_{c_{iso}}} = 0.07$, $\overline{e'_{c_{hex}}} = -0.09$, $\overline{e'_{c_{tet}}} = -0.03$ and $\overline{e'_{c_{ort}}} = -0.02$.

Figure 8 presents the results in terms of their relative error for the elasticity matrices,

$$e_{\|C\|} = \frac{\|C\| - \|C^{target}\|}{\|C^{target}\|}. \quad (19)$$

It can be observed that $\overline{e_{\|C\|}}$ and its dispersion diminish with BV/TV , from $0.3 \lesssim e_{\|C\|} \lesssim 4$ for $BV/TV < 10\%$ to $0.2 \lesssim e_{\|C\|} \lesssim 0.8$ for $BV/TV > 32\%$. At the same time, it is interesting to note that, with only a few exceptions, $e_{\|C\|} > 0$, what implies that the optimized parameterized microstructures are, in general, stiffer than the target natural ones. It might be argued that the parameterized microstructures make, in terms of stiffness, a more efficient use of the material than natural microstructures, being this greater efficiency more noticeable for low BV/TV .

The solutions can be improved for $e_{\|C\|}$ by doing a convenient selection of the Young's modulus of the artificial microstructure material. If the artificial microstructure is constructed using a material with Young's modulus $E' = \frac{\|C^{target}\|}{\|C\|} E$, the error for the elastic matrix norm $e_{\|C\|} = 0$. Clearly, this scaling of the Young's modulus does not affect the elastic symmetries. The above analysis was performed for the 141 samples. The average scaling factor for the Young's modulus was found $\overline{E'/E} = 0.55$ with and standard deviation $SD_{E'/E} = 0.20$. Resultant mean errors and standard deviations for the elasticity coefficients are reported in Table 3. Errors are reported relative to the individual elasticity coefficients,

$$e_{ij}^c = \frac{C_{ij} - C_{ij}^{target}}{C_{ij}^{target}}, \quad (20)$$

and relative to the elasticity matrix norm

$$e_{ij}^{\|c\|} = \frac{C_{ij} - C_{ij}^{target}}{\|C^{target}\|}. \quad (21)$$

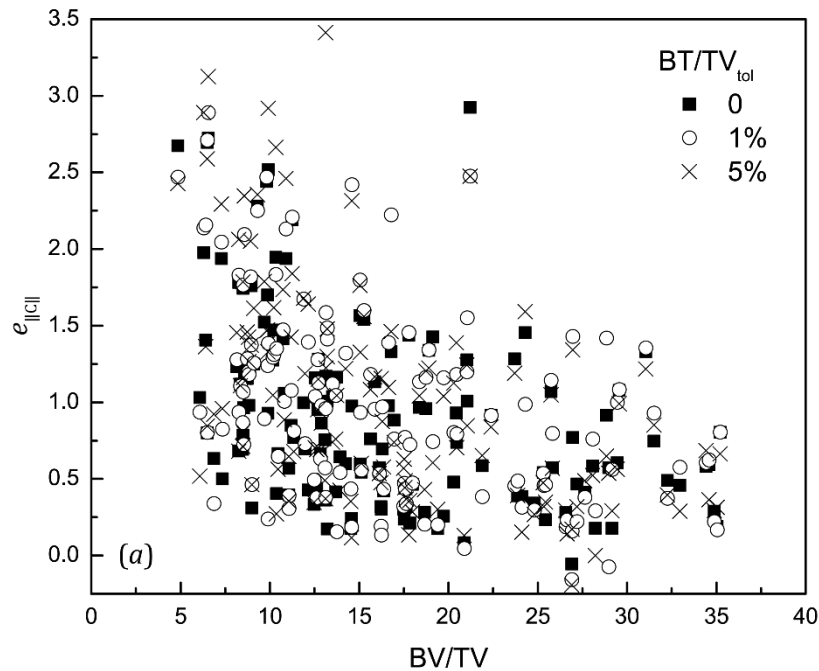


Figure 8: PS optimization of the human samples: stiffness-matrix error as function of BV / TV.

It is observed that coefficients C_{12} , C_{13} and C_{11} have the maximum individual relative errors, which range from 80% to 210%; however, when evaluated relative to $\|C^{target}\|$, maximum errors do not exceed 10%.

Error		Relative errors for elasticity matrix coefficients								
		C_{11}	C_{22}	C_{33}	C_{23}	C_{13}	C_{12}	C_{44}	C_{55}	C_{66}
e_{ij}^c	mean	0.80	-0.04	-0.24	0.34	0.86	2.15	-0.28	0.05	-0.21
	SD	1.06	0.34	0.26	0.66	0.83	1.49	0.38	0.54	0.81
$e_{ij}^{\ c\ }$	mean	0.10	-0.02	-0.11	0.01	0.04	0.08	-0.04	0.00	-0.01
	SD	0.13	0.08	0.14	0.03	0.03	0.03	0.04	0.03	0.04

Table 3: Relative errors for the elasticity matrix after the PS optimization.

5.2 Bovine specimens

The optimization was performed for the orthotropic part of the stiffness matrices of the 5 bovine specimens from Colabella et al. (2017). Tolerance for the volume fraction was set $BV/TV_{tol} = 1\%$. The optimized microstructures are shown in Figure 9 together with their corresponding target natural samples. Table 5 and Table 6 report the errors for the symmetry classes and the elasticity coefficients, respectively. Error for the symmetry classes are in relation to the ranges of the extreme fractions for the bovine microstructures in Table 1 as in equation (18).

Table 5 shows that, with the only exception of the tetragonal symmetry, errors for the symmetry classes are very low. The large relative errors for the tetragonal symmetry are

explained due to its small relative contribution to the elasticity matrix. The worst performance is for Sample #2, which has the particularity of having the lowest isotropic class and the highest orthorhombic class fractions, $c_{iso} = 0.54$ and $c_{ort} = 0.27$, respectively.

Error for the elasticity coefficients are in Table 6. They were computed after the scaling of the Young's modulus to make $e_{||C||} = 0$. The resultant scaling factors range $0.41 < E'/E < 0.72$ with a mean value of $\overline{E'/E} = 0.55$, which coincides with that of the human sample analysis in the previous section. It is observed that as for the human samples, C_{12} presents the highest mean error level (around 9%); maximum errors are of around 17% for C_{11} and C_{22} of Sample #5.

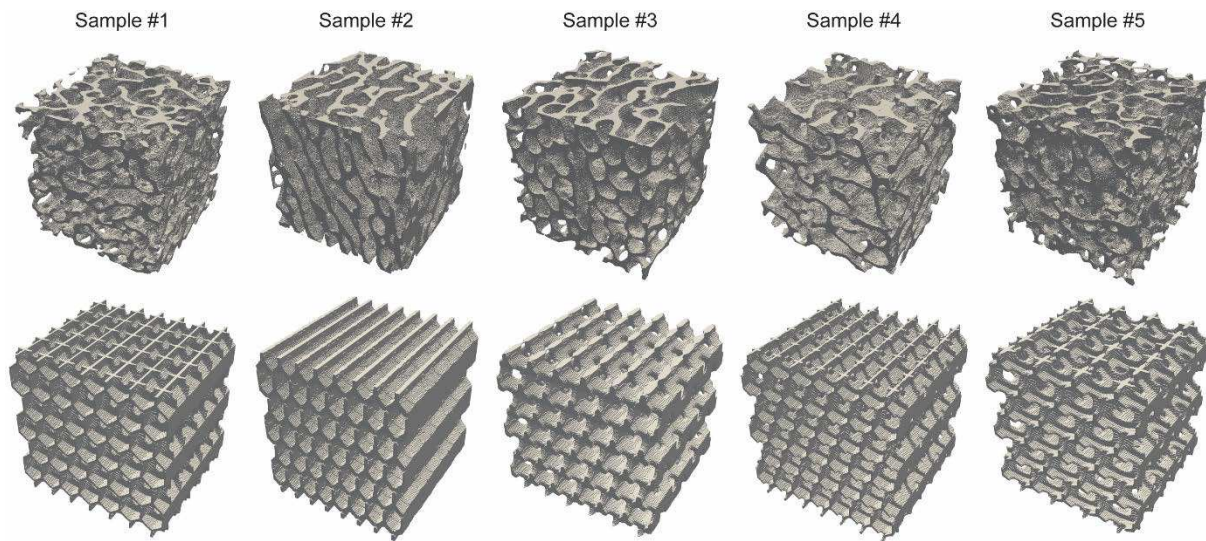


Figure 9: Natural bovine specimens and their mimetic parameterized microstructures.

Sample	Errors for symmetry classes			
	$e'_{c_{iso}}$	$e'_{c_{hex}}$	$e'_{c_{tet}}$	$e'_{c_{ort}}$
1	0.002	0.011	-0.076	0.018
2	0.024	0.166	0.332	-0.696
3	0.001	0.006	-0.049	0.013
4	-0.002	-0.010	0.074	-0.019
5	-0.001	-0.006	0.039	-0.004

Table 4: Errors for the symmetry classes of the mimetic bovine samples.

Sample	Relative errors for elasticity matrix coefficients								
	C_{11}	C_{22}	C_{33}	C_{23}	C_{13}	C_{12}	C_{44}	C_{55}	C_{66}
1	0.034	0.016	-0.008	-0.039	-0.047	0.118	-0.028	-0.082	-0.032
2	0.060	-0.016	-0.018	0.007	0.012	0.065	-0.007	0.015	-0.072
3	-0.004	0.041	-0.035	0.005	0.003	0.048	-0.016	0.009	-0.054
4	0.020	0.034	-0.048	0.029	0.014	0.087	-0.023	-0.001	-0.092
5	0.167	-0.168	-0.039	-0.101	0.047	0.143	-0.062	0.003	-0.009

Table 5: Relative errors for the elasticity matrix of the mimetic bovine samples.

6 CONCLUSIONS

This work introduces a procedure for the design of artificial parameterized microstructures that mimic the elastic response of cancellous bone. The procedure is based on the parameterized

microstructure by Kowalczyk (2006), the geometric parameters of which are optimized to minimize the differences between the symmetry classes of the target and the artificial microstructure elastic tensor.

Symmetry class analyses of experimental data from Kabel et al. (1999a, 1999b) and of specimens processed as part of this work show that elastic symmetries can be related to the specimen BV/TV. The isotropic symmetry class constitutes the main fraction of the elastic tensor; it increases linearly with the specimen bone volume fraction, from around 50% for BV/TV = 5% to 70% for BV/TV = 35%. The isotropic and hexagonal classes add to a constant, such that they account for around 82% of the elastic tensor over the complete BV/TV range. The orthotropic symmetry, given by the addition of the isotropic, hexagonal, tetragonal and orthorhombic classes, constitute around 93% of the elastic tensor, independently of the BV/TV.

The parameterized artificial microstructure is orthotropic by construction. It is shown in this work that it has the capability to combine the isotropic, hexagonal, tetragonal and orthorhombic symmetry classes in the proportions present in the cancellous bone. Analytical expressions for the elastic matrix in terms of the microstructure geometrical parameters are provided.

An optimization strategy is proposed to find the parameterized microstructure that better mimics the elastic response of a target natural bone specimen. The strategy is based on Pattern Search algorithm that uses the geometrical parameters as design variables to minimize the difference between the elastic symmetry classes of artificial and natural microstructures. The analyses of 146 natural cancellous bone specimens resulted in mimetic microstructures whose symmetry class decompositions differ on average 6% with respect to the target values.

The results for the elasticity matrix error allows to observe that the optimized microstructures are in general stiffer than their natural counterparts; this behavior is more noticeable for low BV/TV. This deviation can be compensated by selecting the Young's modulus for the optimized microstructure material such that norm of the difference between elasticity matrices of the target and optimized microstructure vanishes. Clearly, the Young's modulus scaling does not affect the elastic symmetries. The mean value for such scaling factor was found equal to 0.55, i.e., the parameterized microstructure material should have, in average, half the stiffness of the trabecular bone tissue. After scaling, average errors between the optimized and target elasticity matrix coefficients do not exceed 10% relative to the matrix norm.

ACKNOWLEDGEMENTS

This work has been supported by projects PIRSES-GA2009_246977 "Numerical Simulation in Technical Sciences" of the Marie Curie Actions FP7-PEOPLE-2009-IRSES of the European Union and by the PICS project "Modeling and Simulation in Multidisciplinary Engineering" MoSiMe funded in the framework of the CAFCI call by CONICET (Argentina) and CNRS (France). This project has received funding from the European Research Council (ERC) under the European Union's Horizon 2020 research and innovation program (grant agreement No 682001, project ERC Consolidator Grant 2015 BoneImplant).

REFERENCES

- Browaeys J T, Chevrot S, Decomposition of the elastic tensor and geophysical applications. *Geophys J Int* ,159:667–678, 2004.
- Carretta R, Lorenzetti S, Müller R, Towards patient-specific material modeling of trabecular bone post-yield behavior. *Int J Numer Method Biomed Eng* 29:250–272, 2013.
- Colabella L, Ibarra Pino A A, Ballarre J, Kowalczyk P and Cisilino A P, Calculation of Cancellous Bone Elastic Properties with the Polarization-based FFT Iterative Scheme,

- Computer Methods in Biomechanics and Biomedical Engineering, in press, 2017.
- Cowin S C and Mehrabadi M, On the identification of material symmetry for anisotropic elastic materials. *Q J Mech Appl Math*, 40:451–476, 1987.
- Kabel J, Odgaard A, van Rietbergen B, Huiskes R, Connectivity and the elastic properties of cancellous bone. *Bone* 24:115–120, 1999a.
- Kabel J, van Rietbergen B, Odgaard A, Huiskes R, Constitutive relationships of fabric, density, and elastic properties in cancellous bone architecture. *Bone* 25:481–486, (1999b).
- Keaveny T M, Guo X E, Wachtel E F, et al Trabecular bone exhibits fully linear elastic behavior and yields at low strains. *J Biomech.*, 27(9), 1127–1136, 1994.
- Kowalczyk P, Orthotropic properties of cancellous bone modelled as parameterized cellular material. *Comput Methods Biomech Biomed Engineering*, 9:135–147, 2006.
- Kowalczyk P, Simulation of orthotropic microstructure remodelling of cancellous bone. *J Biomech*, 43:563–569, 2010.
- Stauber M, Müller R, Age-related changes in trabecular bone microstructures: global and local morphometry. *Osteoporos Int*, 17:616–626, 2006a.
- Stauber M, Müller R (2006b) Volumetric spatial decomposition of trabecular bone into rods and plates - A new method for local bone morphometry. *Bone*, 38:475–484, 2006b.
- Walker A M and Wookey J, MSAT-A new toolkit for the analysis of elastic and seismic anisotropy. *Comput Geosci*, 49:81–90, 2012.
- Yang G, Kabel J, Van Rietbergen B, et al, The anisotropic Hooke's law for cancellous bone and wood. *J Elast*, 53:125–46, 1998.